

Correlated Dirac semimetal states in nonsymmorphic $M\text{IrO}_3$ ($M=\text{Sr}, \text{Ba}$ and Ca)

Zhi-Ming Yang¹ and Huan Li^{1,*}

¹College of Physics and Electronic Information Engineering,
Guilin University of Technology, Guilin 541004, China

(Dated: May 20, 2025)

Nonsymmorphic symmetries can give rise to Dirac semimetal (DSM) states. However, few studies have been conducted on DSMs in interacting systems. Here, we induce interacting DSM states in nonsymmorphic iridium oxides SrIrO_3 , BaIrO_3 and CaIrO_3 , and contend that the interaction of electron-electron correlations, strong spin-orbital coupling, and symmetry protection can drive robust and exotic DSM states. Based on the density functional theory combined with dynamical mean-field theory (DFT + DMFT), with the Coulomb interaction parameters computed through doubly screened Coulomb correction approach, we discover that the Dirac fermions are constituted by the strongly spin-orbital coupled $J_{\text{eff}} = 1/2$ states resulting from t_{2g} orbitals of Ir, with significant mass enhancement. Moreover, the nonsymmorphic symmetries induce topological surface bands and Fermi arcs on the (001) surface, which are well separated from bulk states. Our findings establish nonsymmorphic iridium oxides as correlated DSMs under strong electron-electron and spin-orbital interactions.

I. INTRODUCTION

Topological semimetals, encompassing Dirac semimetals and Weyl semimetals, constitute a class of topological states that have garnered widespread attention [1–4]. For these topological semimetals, the involvement of electronic correlations frequently has a significant impact on the behavior of Dirac or Weyl quasi-particles, giving rise to novel transport behaviors such as giant spontaneous Hall effect, thus making the search for topological nodes rather arduous [5–8]. Consequently, there are scarce reports of interacting Dirac semimetals in real materials [9], and the search for Dirac semimetals in correlated materials holds both theoretical and experimental significance.

In $5d$ transition metal compounds, the intensities of electronic correlation, crystal field splitting, and spin-orbit coupling (SOC) are comparable. Under the combined influence of these interactions, the system demonstrates various distinctive behaviors. For instance, in iridium salts, the Ir- $5d$ electrons have a strong SOC, which leads to the recombination and splitting of the t_{2g} energy level in the oxygen octahedron into two orbitals with effective angular momenta of $J_{\text{eff}}=1/2$ and $3/2$ [10]. Here, the $J_{\text{eff}}=1/2$ orbital is half-filled and is readily influenced by electron correlation. The calculation based on the dynamic mean-field theory (DMFT) indicates that in numerous iridium salts, the $J_{\text{eff}}=1/2$ orbital is inclined to undergo Mott transition and even magnetic phase transition [11–14]. Thus, $5d$ transition metal compounds can act as ideal research platform for various competitive interactions.

Theoretical and experimental studies have revealed that nonsymmorphic symmetry can generate band overlap at certain high symmetry points in the Brillouin zone [15]. With the introduction of SOC, these quadruple-degenerate points can support Dirac nodes [16–19]. For some nonsymmorphic materials of iridium oxides, due to their strong SOC, they can also hold Dirac semimetal states [20]. Moreover, the pres-

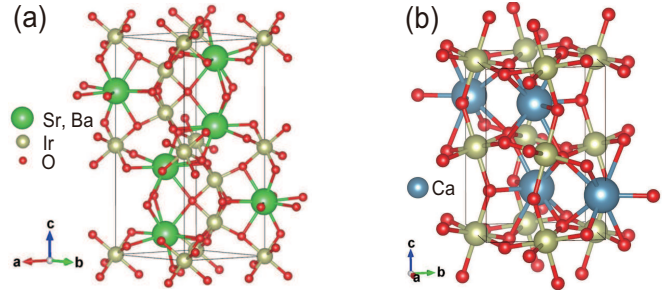


FIG. 1: Crystal structures of iridium oxides (a) SrIrO_3 , BaIrO_3 , and (b) CaIrO_3 .

ence of strong electron correlation in iridium oxides can hold Dirac quasiparticles with strong correlation character [21]. In this context, we ascertained that three iridium oxides SrIrO_3 , BaIrO_3 and CaIrO_3 possessing nonsymmorphic symmetries can serve as ideal platforms for the study of correlated Dirac semimetals. We employed the DFT + DMFT theory to calculate the electronic correlations and discovered that a strong SOC was capable of reorganizing the electron orbitals near the Fermi level to generate $J_{\text{eff}} = 1/2$ orbital and produce Dirac nodes at certain high symmetry points in the Brillouin zone under the protection of nonsymmorphic symmetries. Furthermore, these Dirac quasi-particles display a significant mass enhancement effect, reflecting their interacting intrinsicity. We also found that the surface states of SrIrO_3 and BaIrO_3 are well separated from the bulk states, featuring robust surface-state Fermi arcs that can be observed in future experiments.

II. CRYSTAL STRUCTURE AND COMPUTATIONAL METHODS

Fig.1 depicts the crystal structures of SrIrO_3 , BaIrO_3 and CaIrO_3 . SrIrO_3 and BaIrO_3 pertain to the monoclinic crystal structure with $C2/c$ space group (no. 15) [21] and can be regarded as being distorted from the hexagonal perovskite structure. Evidently, this lattice structure possesses nonsym-

*Electronic address: lihuan@glut.edu.cn

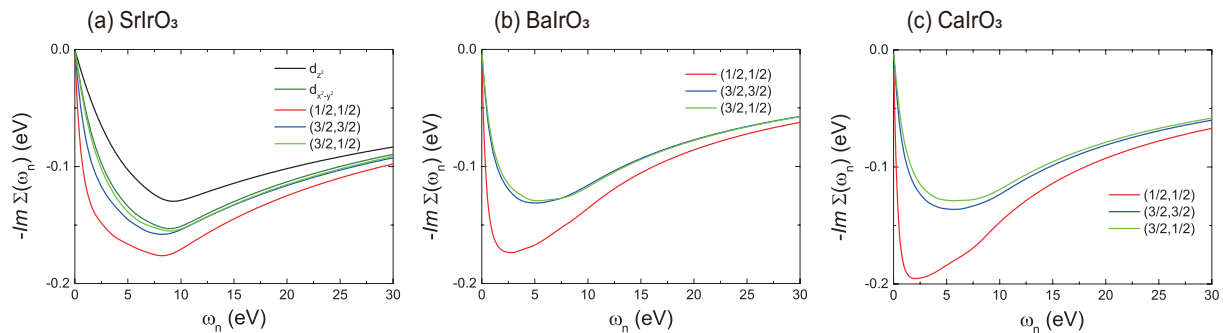


FIG. 2: DFT+DMFT self-energies of (a) SrIrO₃ and (b) BaIrO₃ at 116 K. The self-energies of different orbitals are displayed with lines of different colors.

morphic symmetries, namely gliding mirror planes and screw axes. Specifically, the glide plane lies on the plane expanded by the vectors $\mathbf{a} + \mathbf{b}$ and \mathbf{c} , and the glide vector is $(0, 0, 1/2)$. CaIrO₃ crystallizes in an orthorhombic perovskite structure, with $pnma$ space group (no. 62) [22], and possesses multiple glide planes and screw axes [23]. The $5d$ transition metal compounds iridates possess a strong SOC in Ir atoms, under the influence of SOC, the nonsymmorphic lattice symmetries can permit the emergence of Dirac nodes at some high-symmetric points in the Brillouin zone, as will be discussed in the following text.

To further explore the impact of electronic correlation on iridium oxides, our study adopted a combined approach of density functional theory (DFT) and dynamical mean-field theory (DMFT), and employed the EDMFT software package for such computations [24]. In the DFT section, we utilized the WIEN2k code to generate the Kohn-Sham single-particle Hamiltonian \mathbf{H}_{KS} via the full-potential linear augmented plane-wave method [25]. Subsequently, this Hamiltonian was combined with the interaction term \mathbf{H}_{int} and the double-counting term \sum_{dc} to obtain the lattice model $\mathbf{H}_{\text{DFT+DMFT}} = \mathbf{H}_{\text{KS}} + \mathbf{H}_{\text{int}} - \sum_{\text{dc}}$. The DMFT algorithm projected the states within an energy window $[-10, 10]$ eV relative to the Fermi level in the lattice model onto a single-site Anderson impurity model and employed the hybridization expansion version of continuous-time quantum Monte Carlo (CT-QMC) method to solve this impurity model. To acquire the real-frequency self-energy of $5d$ electrons, the maximum-entropy method was utilized for analytical continuation, converting the complex-frequency results obtained through CT-QMC simulations into real frequencies. The iterative DFT+DMFT calculation approach enables the achievement of complete charge self-consistency, and this computational method has been extensively applied in the investigation of electronic correlations in transition metal compounds [11, 14, 26, 27].

In the DFT portion, a $15 \times 15 \times 6\mathbf{k}$ grid was employed for the integration of the Brillouin zone, and the cutoff parameter K_{max} was set according to $R_{\text{MT}} K_{\text{max}} = 7.0$. Additionally, SOC was consistently incorporated into the calculations as it plays a crucial role in the electronic structure of iridates. To validate the accuracy and reliability of the DFT band structure, the VASP code was utilized for cross-validation. To

better conform to experimental observations, specific values of local Coulomb repulsion energy U and the Hund coupling J were adopted via doubly screened Coulomb correction approach (DSCC) [28], which are in accordance with previous literature reports of related iridium oxides [11, 26, 29]. Furthermore, we also utilized various values of U and J to examine the degree of dependence of electron correlation on the electronic structure. The double-counting term was implemented in a nominal manner, namely $\sum_{\text{dc}} = U(n_f - 1/2) - J/2(n_f - 1)$, where n_f represents the average occupancy of the Ir- $5d$ orbitals, which is approximately 5 in iridates. Each iteration of the DFT+DMFT process consists of one DMFT calculation followed by 20 DFT calculations. In each CT-QMC computation, a total of 128 CPU cores were utilized to execute a significant number of (10×10^8) QMC steps. Typically, after approximately 30 to 40 iterations of the combination of DFT and DMFT, the self-consistency condition is attained, followed by five additional iterations to further average the self-energies.

III. SPIN-ORBIT COUPLING AND ELECTRONIC CORRELATIONS

In iridates, under the crystal field effect of the IrO₆ octahedrons, the d orbitals of Ir are split into e_g and t_{2g} orbitals. The e_g orbitals are doubly degenerate with a relatively high energy, while the t_{2g} orbitals are triply degenerate and their energy levels are close to the Fermi energy. However, since the strength of SOC in iridates is comparable to that of the crystal field, the t_{2g} orbitals will be reorganized into three orbitals, with effective angular momenta of $(J_{\text{eff}}, J_z) = (1/2, \pm 1/2)$, $(3/2, \pm 3/2)$, and $(3/2, \pm 1/2)$, respectively [10]. Near the Fermi level, the $J_{\text{eff}} = 1/2$ orbital dominates and can be significantly influenced by Coulomb correlations, resulting in the singular effects such as Mott transitions or magnetic phase transitions [11–14, 26, 30–34].

We employed the Wien2k software to calculate the DFT electron bands of MIrO₃ (M=Sr, Ba, and Ca) and carried out bidirectional verification using the VASP package. It can be observed from Fig. 3(a) to (c) that, due to nonsymmorphic symmetry, band crossings occur at the M and A points in SrIrO₃ and BaIrO₃, while for CaIrO₃, the band crossings take

TABLE I: Mass enhancement $\frac{m^*}{m_{\text{DFT}}}$ of Dirac quasi-particles under DFT+DMFT simulations at 116 K, with $(U, J)_{\text{DSCC}}=(2.16, 0.61)$, $(2.37, 0.64)$ and $(2.42, 0.63)$ eV for SrIrO₃, BaIrO₃ and CaIrO₃, respectively. For comparison, larger values of U and J are also employed in DFT+DMFT calculation.

(U, J)	use DSCC	use (4.5, 0.8) eV	Exp.
SrIrO ₃	1.25	1.63	1.4 [21]
BaIrO ₃	1.49	2.89	-
CaIrO ₃	1.53	3.12	-

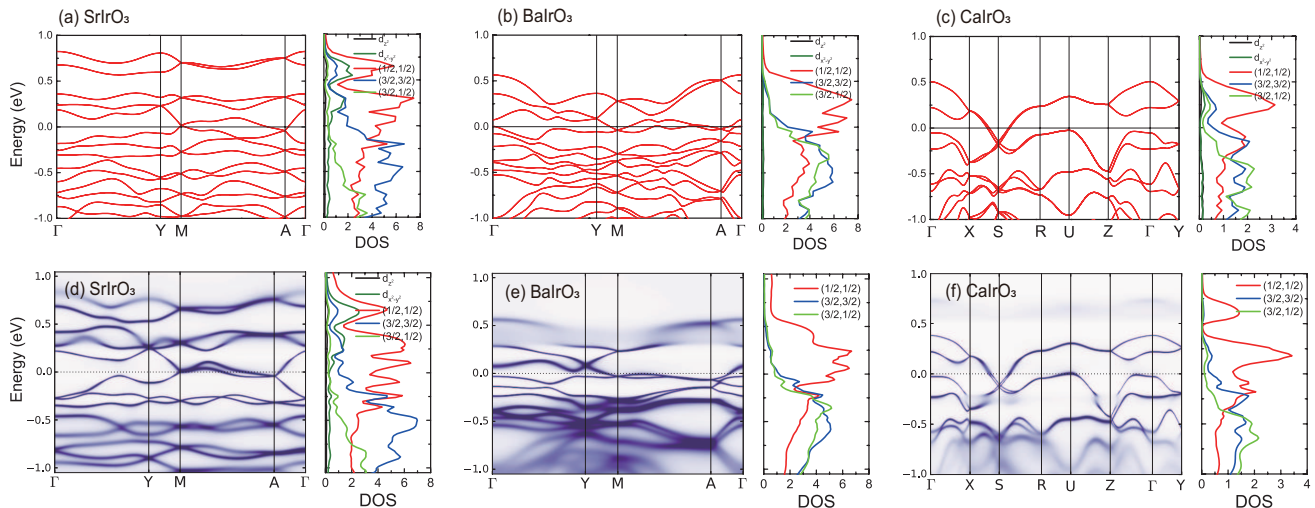


FIG. 3: (a), (b) and (c) represent the DFT energy bands of SrIrO₃, BaIrO₃ and CaIrO₃ respectively, while (d) to (f) represent their DFT+DMFT spectral functions. The right panel in each graph shows the corresponding partial density of states projected into (J_{eff}, J_z) states.

TABLE II: Temperature dependence of mass enhancement of Dirac quasi-particles using $(U, J)_{\text{DSCC}}$ in DFT+DMFT simulations.

Temperature (K)	116	400
SrIrO ₃	1.25	1.24
BaIrO ₃	1.49	1.46
CaIrO ₃	1.53	1.55

place near S point. Given that the lattices possess spatial inversion symmetry, each band is doubly degenerate under the SOC effect. Hence, these crossing points are quadruply degenerate Dirac points [15]. To analyze the orbital components near the Dirac points, we diagonalized the matrix of impurity levels corresponding to the d electrons, thereby obtaining the correct impurity orbitals near the Fermi level, namely (J_{eff}, J_z) states, and expressed them as a linear combination of spheric harmonics, enabling us to obtain the partial DOS of the (J_{eff}, J_z) orbitals [24]. The results are presented in the smaller plots on the right panels in Fig. 3(a) to (c). It can be discerned that due to the interplay between SOC and the crystal-field splitting, the DOS near the Fermi level is mainly composed by the $(J_{\text{eff}}, J_z) = (1/2, 1/2)$ state, with a small amount of $(3/2, 3/2)$ component (approximately half of the $(1/2, 1/2)$ component), while the contributions from the re-

maining orbitals ($(3/2, 1/2)$ and the two e_g orbitals) are essentially negligible. Compared with $J_{\text{eff}} = 3/2$ orbitals that are almost completely filled, the $J_{\text{eff}} = 1/2$ orbital is essentially half-filled, thus the occupation of $5d$ electrons is 5 (i.e., t_{2g}^5 configuration), corresponding to Ir⁴⁺ valence. Therefore, $J_{\text{eff}} = 1/2$ orbital is more susceptible to Coulomb correlation, and may induce the Mott transition and magnetic transition in some iridates [11–14, 26, 30–34].

To investigate the consequence of d -electron Coulomb correlation on the Dirac quasiparticles in SrIrO₃, BaIrO₃ and CaIrO₃, we adopted the DFT + DMFT algorithm [24] and calculated the self-energies of each d orbitals. The Coulomb interaction parameters, such as on-site Coulomb repulsion U and Hund's coupling J , play a crucial role in the DFT + DMFT simulation. To calculate these parameters efficiently and precisely, we utilized the doubly screened Coulomb correction approach [28]. The calculation results are $(U, J) = (2.16, 0.61)$, $(2.37, 0.64)$ and $(2.42, 0.63)$ eV for SrIrO₃, BaIrO₃ and CaIrO₃. The larger lattice parameters of BaIrO₃ compared to SrIrO₃ enhances the localization of Ir- $5d$ electrons and consequently leads to an larger Hubbard parameter U . It can be noted that the obtained values are comparable to that adopted by the constrained random phase approximation (cRPA) method for Sr₂IrO₄ and Ba₂IrO₄ [11, 26, 29]. The correlation effect can be gauged by the mass enhancement factor $Z = \frac{m^*}{m_{\text{DFT}}} = 1 - \frac{\partial \text{Im}\Sigma(\omega_n)}{\partial \omega_n} \Big|_{\omega_n \rightarrow 0}$. As can

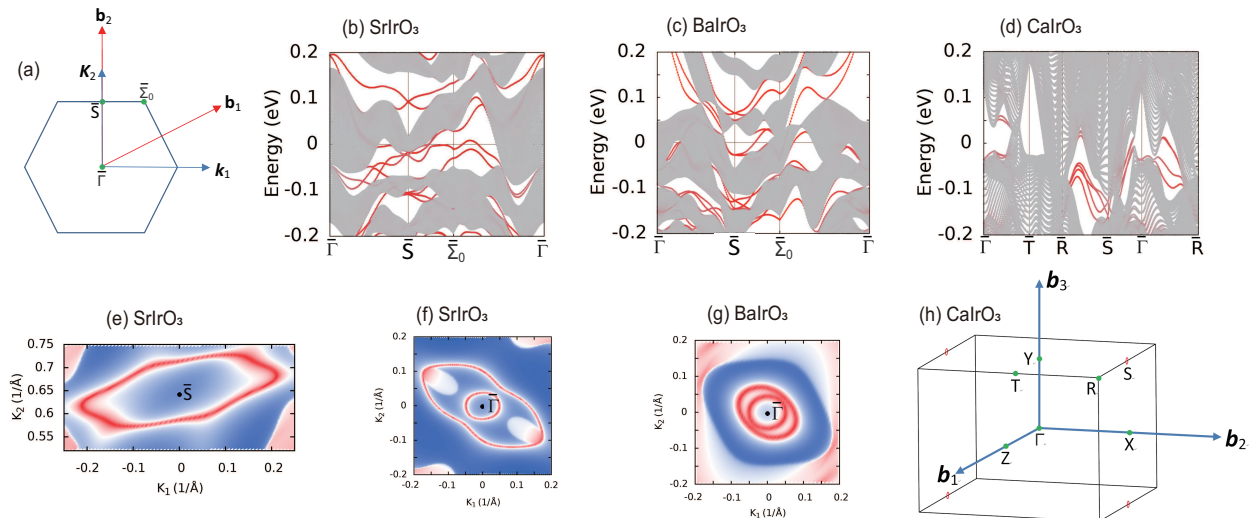


FIG. 4: (a) The (001) surface Brillouin zone of SrIrO₃ and BaIrO₃. (b) to (d) represent the slab energy spectra of SrIrO₃, BaIrO₃ and CaIrO₃ respectively, among which the red lines denote the surface states. (e) and (f) show the surface-state Fermi arcs of SrIrO₃ emerging near the \bar{S} and $\bar{\Gamma}$ points, at a energy cut at 0.11 eV and 0.18 eV, respectively. (g) The surface-state Fermi arcs of BaIrO₃ emerging near the $\bar{\Gamma}$ point, at a energy cut at 0.254 eV. (h) Dirac node rings of CaIrO₃, which are denoted by small red circles near the Brillouin zone boundaries.

be seen from Fig. 2, the $J_{\text{eff}} = 1/2$ orbital in both iridates has a more pronounced mass enhancement than other orbitals. Moreover, the mass enhancement of $J_{\text{eff}} = 1/2$ orbital in isomorphous BaIrO₃ is stronger than that of SrIrO₃ ($Z=1.49$ vs 1.25), demonstrating that the correlation effect of Dirac quasiparticles is more remarkable in BaIrO₃. In addition, we evaluated the mass enhancement factors across a range of temperatures and observed that their variation with temperature was relatively smooth, exhibiting only a minor increase upon cooling, see Tab. II. Consequently, the mass enhancement result at 116 K is sufficiently representative of the characteristics under low-temperature conditions.

In some DFT+DMFT studies, larger correlation parameters U were employed for the calculations of iridates and ruthenium trihalides [13]. To systematically investigate the impact of the choice of correlation parameters on DFT+DMFT calculations, we evaluated the mass enhancement factor under increased $U = 4.5$ eV. The detailed results are presented in Tab. I. It is evident that this leads to a substantially stronger mass enhancement. Consequently, our DFT+DMFT simulations based on DSCC results demonstrate a higher level of agreement with the experimental data, which further validates the accuracy of the correlations parameters derived via DSCC calculations.

The renormalization of quasiparticles can be directly perceived from the spectral function presented in Fig. 3(d) to (f). Near the Fermi level, the momentum-resolved spectral function of SrIrO₃ shows minor deviations from the DFT band in Fig. 3(a), indicating a relatively small mass enhancement of the Dirac quasiparticles near the Dirac points at M and A. However, as can be seen from the spectral function of BaIrO₃, the dispersion at the Dirac points is strongly compressed, suggesting a significant mass enhancement for the Dirac quasiparticles. Additionally, the introduction of Coulomb corre-

lation causes a notable change in the partial DOS near the Dirac points: the components of $J_{\text{eff}} = 1/2$ orbital in SrIrO₃, BaIrO₃ and CaIrO₃ increase significantly, while the contributions of the other orbitals are significantly suppressed compared to the results of DFT. This indicates that these Dirac quasiparticles are almost entirely composed of the orbital with $J_{\text{eff}} = 1/2$.

IV. TOPOLOGICAL SURFACE STATES

Dirac semimetals can generate observable topological surface states. For instance, on certain surfaces of Na₃Bi and Cd₃As₂, Fermi arcs connect two Dirac points and form closed loops, which are significantly different from the non-closed Fermi arcs in Weyl semimetals [3, 4, 35]. To investigate the surface-state characteristics of SrIrO₃, BaIrO₃, and CaIrO₃, we constructed their tight-binding models using the Wannier90 software package [36] and calculated the electronic dispersion relations of 60-layer thin films with (001) surfaces using the WannierTools software package [37]. The results are shown in Figs. 4(b) to (d), where the gray and red lines correspond to the energy spectra of the bulk and surface states, respectively. For SrIrO₃ and BaIrO₃, the Brillouin zone of their (001) surfaces is shown in Fig. 4(a). On this surface, the Dirac points M and A (and their equivalent points along the k_z direction) of the bulk state project onto the \bar{S} and $\bar{\Gamma}$ points, respectively. Therefore, both the \bar{S} and $\bar{\Gamma}$ points are the projection overlap points of two equivalent Dirac points. All points on the $\bar{\Gamma}$ -A path of the bulk state project onto the $\bar{\Gamma}$ point of the (001) surface. Thus, as can be seen from Figs. 4(b) and (c), the bulk state at the $\bar{\Gamma}$ point covers a relatively large energy range above and below the Fermi level (reflecting the energy dispersion of the bulk band along the k_z direction,

corresponding to the energy range from the Dirac point A to the Γ point in Figs. 3(a) and (b)), and completely covers the surface state within this range. Only around 0.2 eV above the Fermi level, the surface state is well separated from the bulk state. In contrast, the M-Y path projects onto the \bar{S} point. Due to the smaller energy range of this segment, the energy range covered by the bulk state on the (001) surface is also smaller, thereby exposing some surface state dispersions that are not covered by the bulk state.

From Figs. 4 (b) and (c), it can be observed that at the \bar{S} and $\bar{\Gamma}$ points in the (001) surface Brillouin zone, the surface states intersect, forming closed Fermi arcs. This phenomenon can be intuitively demonstrated by the surface Fermi surface patterns of SrIrO₃ and BaIrO₃ shown in Figs. 4(e) to (g). Similar surface states and Fermi arcs have also been observed in other Dirac nodal line semimetals, such as CeSbTe and Zr-SiS [19, 38]. Additionally, we found that the dispersion characteristics of these surface states are independent of the number of layers in the slab structure, indicating that these surface states are robust and topologically protected. For CaIrO₃, its Dirac nodal rings are small and are located near the S point on the bulk Brillouin zone boundary (see Fig. 4(h)). The energy dispersion of CaIrO₃ on the (001) surface is shown in Fig. 4(d), where multiple surface states appear in the projected area near the \bar{S} point.

V. CONCLUSION

Based on the Coulomb correlation parameters self-consistently calculated using the doubly screened Coulomb correction approach, this study employs a combined approach of density functional theory (DFT) and dynamical mean-field theory (DMFT) to systematically investigate the electronic structure and topological quantum states of MIrO₃ (M=Sr, Ba and Ca) compounds with nonsymmorphic symmetries.

Through diagonalization analysis of the matrix of impurity levels for Ir-5d orbitals, it is revealed that under the synergistic effect of strong spin-orbit coupling (SOC) and crystal fields in Ir-5d states, orbital state reconstruction occurs, forming characteristic orbitals with an effective angular momentum of $J_{\text{eff}} = 1/2$. These orbital components constitute the dominant contribution to the energy bands near the Fermi level. DFT+DMFT calculations demonstrate that Coulomb correlation effects significantly enhance the weight proportion of $J_{\text{eff}} = 1/2$ states in the energy bands around the Fermi energy. Further investigations show that regulated by the nonsymmorphic symmetries of the MIrO₃ lattices, $J_{\text{eff}} = 1/2$ states form Dirac nodes near specific high-symmetry points in the Brillouin zone. Quasiparticle effective mass calculations based on DFT+DMFT indicate that these Dirac quasiparticles exhibit weakly correlated characteristics, with their dynamic behavior being in excellent agreement with experimental measurements. Additionally, through tight-binding model simulation of surface states, it is found that near high-symmetry points in the surface Brillouin zone, surface states are clearly decoupled from bulk states, forming closed surface Fermi arc structures. This work clarifies that in MIrO₃ systems with nonsymmorphic symmetries, the synergistic effects of symmetry protection, strong spin-orbit coupling, and electron correlations can induce unique topological states, providing a theoretical reference for the investigation of exotic correlated topological materials.

Acknowledgments

H. Li acknowledges the supports from National Natural Science Foundation of China (No. 12364023), and Guangxi Natural Science Foundation (No. 2024GXNS-FAA010273).

-
- [1] B. Q. Lv, H. M. Weng, B. B. Fu, X. P. Wang, H. Miao, J. Ma, P. Richard, X. C. Huang, L. X. Zhao, G. F. Chen, Z. Fang, X. Dai, T. Qian, and H. Ding, *Phys. Rev. X* **5**, 031013 (2015).
- [2] Z. Wang, K. Luo, J. Zhao, and R. Yu, *Phys. Rev. B* **100**, 205117 (2019).
- [3] Zhijun Wang, Yan Sun, Xing-Qiu Chen, Cesare Franchini, Gang Xu, Hongming Weng, Xi Dai, and Zhong Fang, *Phys. Rev. B* **85**, 195320 (2012).
- [4] Zhijun Wang, Hongming Weng, Quansheng Wu, Xi Dai, and Zhong Fang, *Phys. Rev. B* **88**, 125427 (2013).
- [5] H.-H. Lai, S. E. Grefe, S. Paschen, and Q. Si, *Proc. Natl. Acad. Sci. USA* **115**, **93** (2018).
- [6] C. Cao, G.-X. Zhi, and J.-X. Zhu, *Phys. Rev. Lett.* **124**, 166403 (2020).
- [7] A. Kofuji, Y. Michishita, and R. Peters, *Phys. Rev. B* **104**, 085151 (2021).
- [8] S. Dzsaber, X. Yan, M. Taupin, G. Eguchi, A. Prokofiev, T. Shiroka, P. Blaha, O. Rubel, S. E. Grefe, H.-H. Lai, Q. Si, and S. Paschen, *Proc. Natl. Acad. Sci. USA* **118**, e2013386118 (2021).
- [9] Hao-Tian Ma, Xing Ming, Xiao-Jun Zheng, Jian-Feng Wen, Yue-Chao Wang, Yu Liu, and Huan Li, *Phys. Rev. B* **107**, 075124 (2023).
- [10] B. J. Kim, Hosub Jin, S. J. Moon, J.-Y. Kim, B.-G. Park, C. S. Leem, Jaejun Yu, T.W. Noh, C. Kim, S.-J. Oh, J.-H. Park, V. Durairaj, G. Cao, and E. Rotenberg *Phys. Rev. Lett.* **101**, 076402 (2008).
- [11] Hongbin Zhang, Kristjan Haule, and David Vanderbilt, *Phys. Rev. Lett.* **111**, 246402 (2013).
- [12] S. Fujiyama, H. Ohsumi, T. Komesu, J. Matsuno, B. J. Kim, M. Takata, T. Arima, and H. Takagi, *Phys. Rev. Lett.* **108**, 247212 (2012).
- [13] Subhasis Samanta, Dukgeun Hong, and Heung-Sik Kim, *Nanomaterials* **14**, 9 (2024).
- [14] Gang Cao and Pedro Schlottmann, *Rep. Prog. Phys.* **81**, 042502 (2018).
- [15] S. M. Young and C. L. Kane, *Phys. Rev. Lett.* **115**, 126803 (2015).
- [16] B.-B. Fu, C.-J. Yi, T.-T. Zhang, M. Caputo, J.-Z. Ma, X. Gao, B. Q. Lv, L.-Y. Kong, Y.-B. Huang, M. Shi et al., *arXiv:1712.00782*.

- [17] L. M. Schoop, M. N. Ali, C. Straßer, A. Topp, A. Varykhalov, D. Marchenko, V. Duppel, S. S. P. Parkin, B. V. Lotsch, and C. R. Ast, *Nat. Commun.* **7**, 11696 (2015).
- [18] H. Wu, A. M. Hallas, X. Cai, J. Huang, J. S. Oh, V. Loganathan, A. Weiland, G. T. McCandless, J. Y. Chan, S.-K. Mo et al., *npj Quantum Mater.* **7**, 31 (2022).
- [19] C. Chen, X. Xu, J. Jiang, S.-C. Wu, Y. P. Qi, L. X. Yang, M. X. Wang, Y. Sun, N. B. M. Schröter, H. F. Yang, L. M. Schoop, Y. Y. Lv, J. Zhou, Y. B. Chen, S. H. Yao, M. H. Lu, Y. F. Chen, C. Felser, B. H. Yan, Z. K. Liu, and Y. L. Chen, *Phys. Rev. B* **95**, 125126 (2017).
- [20] T. Takayama, A. N. Yaresko, and H. Takagi, *J. Phys.: Condens. Matter* **31**, 074001 (2018).
- [21] Yu-Te Hsu, Danil Prishchenko, Maarten Berben, Matija Čulo, Steffen Wiedmann, Emily C. Hunter, Paul Tinnemans, Tomohiro Takayama, Vladimir Mazurenko, Nigel E. Hussey, and Robin S. Perry, *npj Quantum Mater.* **6**, 92 (2021).
- [22] Taku Tsuchiya and Jun Tsuchiya, *Phys. Rev. B* **76**, 144119 (2007).
- [23] M. Ahsan Zeb, and Hae-Young Kee, *Phys. Rev. B* **86**, 085149 (2012).
- [24] K. Haule, C.-H. Yee, and K. Kim, *Phys. Rev. B* **81**, 195107 (2010).
- [25] P. Blaha, K. Schwarz, F. Tran, R. Laskowski, G. K. H. Madsen, and L. D. Marks, *J. Chem. Phys.* **152**, 074101 (2020).
- [26] R. Arita, J. Kuneš, A.V. Kozhevnikov, A. G. Eguiluz, and M. Imada, *Phys. Rev. Lett.* **108**, 086403 (2012).
- [27] Peng-Fei Tian, Hao-Tian Ma, Xing Ming, Xiao-Jun Zheng and Huan Li, *J. Phys.: Condens. Matter* **36**, 355602 (2024).
- [28] B.-L. Liu, Y.-C. Wang, Y. Liu, H.-F. Liu, and H.-F. Song, Doubly Screened Coulomb Correction Approach for Strongly Correlated Systems, *J. Phys. Chem. Lett.* **14**, 8930 (2023).
- [29] Hongbin Zhang, Kristjan Haule, and David Vanderbilt, *Phys. Rev. Lett.* **118**, 026404 (2017).
- [30] Yoshinori Imai, Kazuhiro Nawa, Yasuhiro Shimizu, Wakana Yamada, Hideyuki Fujihara, Takuya Aoyama, Ryotaro Takahashi, Daisuke Okuyama, and Takamasa Ohashi et al., *Phys. Rev. B* **105**, L041112 (2022).
- [31] David A. S. Kaib, Kira Riedl, Aleksandar Razpopov, Ying Li, Steffen Backes, Igor I. Mazin, and Roser Valentí *npj Quantum Materials* **7**, 75 (2022).
- [32] Yang Zhang, Ling-Fang Lin, Adriana Moreo, and Elbio Dagotto, *Phys. Rev. B* **105**, 085107 (2022).
- [33] Kazuhiro Nawa, Yoshinori Imai, Youhei Yamaji, Hideyuki Fujihara, Wakana Yamada, Ryotaro Takahashi, Takumi Hiraoka, Masato Hagihara, Shuki Torii, Takuya Aoyama, Takamasa Ohashi, Yasuhiro Shimizu, Hirotada Gotou, Masayuki Itoh, Kenya Ohgushi, and Taku J. Sato, *Journal of the Physical Society of Japan* **90**, 123703 (2021).
- [34] Heung-Sik Kim, Vijay Shankar V., Andrei Catuneanu, and Hae-Young Kee, *Phys. Rev. B* **91**, 241110(R) (2015).
- [35] Bohm-Jung Yang and Naoto Nagaosa, *Nat. Commun.* **5**, 4898 (2014).
- [36] G. Pizzi, V. Vitale, R. Arita, S. Blügel, F. Freimuth, G. Géranton, M. Gibertini, D. Gresch, C. Johnson, T. Koretsune, J. Ibañez-Azpiroz, H. Lee, J. M. Lihm, D. Marchand, A. Marrazzo, Y. Mokrousov, J.I. Mustafa, Y. Nohara, Y. Nomura, L. Paulatto, S. Poncé, T. Ponweiser, J. Qiao, F. Thöle, S.S. Tsirkin, M. Wierzbowska, N. Marzari, D. Vanderbilt, I. Souza, A. A. Mostofi, J. R. Yates, *J. Phys. Cond. Matt.* **32**, 165902 (2020).
- [37] QuanSheng Wu, ShengNan Zhang, Hai-Feng Song, Matthias Troyer, Alexey A Soluyanov, *Computer Physics Communications* **224**, 405 (2017).
- [38] Leslie M. Schoop, Andreas Topp, Judith Lippmann, Fabio Orlandi, Lukas MÜchler, Maia G. Vergniory, Yan Sun, Andreas W. Rost, Viola Duppel, Maxim Krivenkov, Shweta Sheoran, Pascal Manuel, Andrei Varykhalov, Binghai Yan, Reinhard K. Kremer, Christian R. Ast, Bettina V. Lotsch, *Sci. Adv.* **4** eaar2317 (2018).